Adhesion Aspects in MEMS/NEMS

Edited by

S.H. Kim
M.T. Dugger
K.L. Mittal

VSP

Adhesion Aspects in MEMS/NEMS

This page intentionally left blank

Adhesion Aspects in MEMS/NEMS

Edited by

S. H. Kim, M. T. Dugger and K. L. Mittal

LEIDEN • BOSTON
2010

CRC Press
Taylor & Francis Group
6000 Broken Sound Parkway NW, Suite 300
Boca Raton, FL 33487-2742

Version Date: 20120727

International Standard Book Number-13: 978-9-00-419095-5 (eBook - PDF)

Visit the Taylor & Francis Web site at
http://www.taylorandfrancis.com

and the CRC Press Web site at
http://www.crcpress.com

Contents

Part 3: Adhesion and Friction Measurements

Part 4: Adhesion in Practical Applications

Part 5: Adhesion Mitigation Strategies

This page intentionally left blank

Preface

Interfacial interactions between components play a crucial role in the manufacture and performance of MEMS/NEMS devices. This is ascribed to the very large surface-to-volume ratio in such components and, concomitantly, surface/interface phenomena become dominant in controlling the fate of such devices.

Adhesion is an interesting phenomenon. Depending on the situation/application, adhesion may be desideratum and in other situations, it can be an anathema. In the case of MEMS/NEMS devices, static adhesion between components (also known as 'stiction') is something to be avoided for the proper functioning of the device. Avoidance of adhesion constitutes the field of 'abhesion' which in a sense is 'negative adhesion'. In order to achieve abhesion, a plethora of techniques and materials have been developed to mitigate adhesion problems in a wide range of MEMS/NEMS products.

Even a cursory look at the literature will evince that currently there is tremendous R&D activity encompassing many facets (including adhesion) pertaining to MEMS/NEMS products and all signals indicate it will not only continue unabated, but will assume an accelerated pace. The current research emphasis is on the following topics: unraveling interfacial interactions and factors influencing such interactions; ramifications of these interactions in the functioning of devices/structures; developing novel or ameliorating the existing techniques for surface modification to attain desired surface characteristics; and development of various ways to mitigate adhesion problems.

In light of the tremendous relevance of interfacial interactions — and thus adhesion — and flurry of R&D activity in this burgeoning field of MEMS/NEMS products, we decided to make this book available as a single and easily accessible source of comprehensive information. This book is based on the Special Issue of the *Journal of Adhesion Science and Technology* (*JAST*) Vol. 24, Nos 15–16 (2010). The papers as published in the above-mentioned Issue have been grouped in a logical fashion in this book.

This book containing a total of 21 papers (reflecting overviews and original research) and covering many aspects of adhesion in MEMS/NEMS is divided into five parts as follows: Part 1: Understanding Through Continuum Theory; Part 2:

Adhesion Aspects in MEMS/NEMS

Computer Simulation of Interfaces; Part 3: Adhesion and Friction Measurements; Part 4: Adhesion in Practical Applications; and Part 5: Adhesion Mitigation Strategies. Topics covered include: numerical analysis of contact mechanics; equilibrium vapor adsorption and capillary force; contribution of fractal parameters to adhesion; effects of contacting surfaces on MEMS device reliability; adhesion model for micromanipulation; computer simulation of interfaces; vapor phase lubrication in MEMS; atomistic factors governing adhesion; adhesion and friction aspects at the nanoscale; friction of self-assembled monolayers (SAMs); interfacial adhesion and its implications in MEMS/NEMS technology; adhesion in MEMS/NEMS applications; molecular mobility and interface dynamics in organic NEMS; various adhesion mitigation techniques in MEMS/NEMS; superhydrophobic surfaces; plasma modification of polymer surfaces and its relevance in biomedical microdevices.

It is quite patent from the topics covered that many different aspects of adhesion in MEMS/NEMS are accorded due coverage in this book; concomitantly, this book represents a comprehensive treatise on this fascinating, mushrooming and technologically highly important field. Also we would like to point out that this book containing a wealth of information is the first book on the topic of adhesion in MEMS/NEMS. Moreover, we hope this book would serve as a fountainhead for new research ideas and new application vistas will emerge as the performance and durability/robustness of MEMS/NEMS are further enhanced.

This book should be of interest to both neophytes (as a gateway to this field) and veteran researchers as a commentary on the current research activity being carried out by luminaries in this field. An in-depth understanding of adhesion phenomena and development of more effective adhesion mitigation strategies would be a big step in the future of MEMS/NEMS technology.

Acknowledgements

Now it is our pleasure to acknowledge all those who helped in many and varied ways in materializing this book. First and foremost, we profusely thank the authors for their interest, enthusiasm and cooperation, without which this book could not be born. Second, we are most appreciative of the reviewers for their time and efforts in providing invaluable comments which certainly improved the quality of manuscripts. Next and last, our appreciation goes to the staff of Brill (publisher) for giving this book a body form.

SEONG H. KIM
The Pennsylvania State University
Department of Chemical Engineering
University Park, PA 16804-4400, USA

MICHAEL T. DUGGER
Materials Science and Engineering Center
Sandia National Laboratories
Albuquerque, NM 87185-0889, USA

K. L. MITTAL
P.O. Box 1280
Hopewell Jct., NY 12533, USA

This page intentionally left blank

Part 1

Understanding Through Continuum Theory

This page intentionally left blank

Numerical Analysis of Contact Mechanics between a Spherical Slider and a Flat Disk with Low Roughness Considering Lennard–Jones Surface Forces

Kyosuke Ono *

Mechanical Engineering Research Laboratory, Hitachi Ltd., Kirihara-cho 1, Fujisawa-shi, Kanagawa-ken 252-8588, Japan

---

Abstract

Although analytical and numerical analyses of the contact mechanics of a completely smooth sphere–flat contact have been done, the analysis of a realistic sphere–flat contact with a surface roughness whose mean height planes have a spacing greater than the atomic equilibrium distance has not been done thoroughly. This paper is a fundamental study of the elastic contact mechanics due to Lennard–Jones (LJ) intermolecular surface forces between a spherical slider and a flat disk with low roughness whose height is larger than equilibrium distance z_0. First, neglecting the effect of the attractive force at contacting asperities, adhesion contact characteristics of a 2-mm-radius glass slider with a magnetic disk are presented in relation to the asperity spacing σ between mean height planes. Results showed that the contact behavior at a small asperity spacing of $\sim$0.5 nm cannot be predicted either by the Johnson–Kendall–Roberts or Derjaguin–Muller–Toporov theories. Second, contact characteristics of a 1-μm-radius sphere on a flat disk are presented to examine how LJ attractive force at contacting asperities can be evaluated. It was found that the adhesion force of contacting asperity is a function of separation in general, but it becomes almost constant when $\sigma = \sim z_0$. A simple equation to evaluate the LJ attractive pressure of contacting asperities is presented for the rough contact analysis. Third, numerical calculation methods for a sphere–flat contact including LJ attractive forces between the mating mean height planes and contacting asperities are presented. Then, adhesion characteristics of a 2-mm-radius glass slider and magnetic disk are calculated and compared with the previous experimental results of dynamic contact test. It is shown that the calculated LJ adhesion force is much smaller than the experimental adhesion force, justifying that the adhesion force observed at the separation of contact is caused by meniscus force rather than by vdW force.

Keywords

Nanotribology, sphere to flat contact mechanics, van der Waals forces, Lennard–Jones intermolecular forces, roughness effect, head–disk interface

---

* Tel.: +81-0466-98-4185; Fax: +81-0466-98-2119; e-mail: kyosuke.ono.jk@hitachi.com

Adhesion Aspects in MEMS/NEMS

1. Introduction

Adhesion contact characteristics between a perfectly smooth sphere and a flat due to intermolecular forces caused by Lennard–Jones potential have been elucidated well by analytical methods [1–4] and numerical calculation methods [5–7]. However, realistic engineering surfaces have roughness that is larger than the atomic equilibrium distance, even for magnetic head–disk interfaces. Adhesion and friction characteristics of nominally flat rough surfaces on the basis of the Greenwood–Williamson roughness contact model [8] and the Derjaguin–Muller–Toporov (DMT) adhesion model [2] were studied by Chang *et al.* [9] and Stanley *et al.* [10]. As an extension of these theories, Suh and Polycarpou [11] analyzed adhesion characteristics of rough surface contacts for nominally flat mating surfaces. In an asperity contact analysis, Lennard–Jones (LJ) surface forces at contacting and non-contacting asperities were taken into account, but LJ surface force due to mean height planes was not considered. However, it is natural to consider that LJ surface force due to mean height planes plays a dominant role when the spacing between the mean height planes is less than 0.5 nm. In addition, since a current magnetic head slider has an ellipsoidal surface, contact characteristics between a sphere and a flat disk should be analyzed. Even in an experimental measurement of contact characteristics using a simple spherical probe, the probe has a roughness with a height that is usually larger than the atomic equilibrium distance of $\sim$0.2 nm [12]. Thus, the adhesion characteristics between the spherical probe and flat disk would be influenced by the surface roughness. Therefore, contact characteristics between a sphere and a flat with a small roughness have not yet been studied in the history of contact mechanics.

In the field of head–disk interfaces, there has been a long-running argument about whether the attractive force between head and disk is caused by van der Waals (vdW) force [13–15] or meniscus force [16–18]. Ono and Nakagawa [19, 20] measured the dynamic adhesion force that was applied on the slider when 1- and 2-mm-radius glass sliders collided with a magnetic disk with a molecularly thin lubricant layer. They concluded that the adhesion force observed at the instant of separation after a short contact period of 15–30 μs was caused by the meniscus force rather than by vdW force. However, there were criticisms that the meniscus bridge could not be generated quickly enough to have this effect.

One of the motivations of this study was to calculate the vdW attractive force between a spherical glass slider and a magnetic disk and compare it with the experimentally measured value. The glass sphere and magnetic disk used for the experiment had a root-mean-square (rms) roughness heights of $\sim$0.33 and 0.52 nm, respectively. Since this is larger than the atomic equilibrium distance, development of an analytical method for asperity contact mechanics between a sphere and a disk is needed.

A numerical analysis method is presented for rough surface contact characteristics between a sphere and a flat, considering not only elastic deformation and vdW forces of mean height planes of the sphere and disk but also vdW forces of contacting asperities. In prior papers on adhesion of contacting rough surfaces [9–11], adhesion forces of contacting and noncontacting asperities were taken into account based on the DMT theory [2, 3]. In order to elucidate adhesion force of a sphere–flat contact with various scales of asperities more rigorously, fundamental contact characteristics of a 2-mm-radius glass sphere and 1-μm-radius asperity with a disk assuming a constant spacing between mean height planes due to contacting asperities are investigated using a numerical calculation method. In Section 3, an analytical model of asperity contact between a sphere and a disk and the assumptions used in this analysis are described. Then, basic equations and numerical calculation method are explained. In Section 4, contact characteristics between the 2-mm-radius sphere and disk are calculated assuming constant spacing between mean height planes in the contact area but ignoring vdW forces of the contacting asperities. In Section 5, to evaluate the adhesion force of contacting asperities of the rough surface, the contact characteristics between a 1-μm-radius spherical asperity and a disk are calculated assuming small-scale spacing due to a small-scale asperity height on the order of atomic equilibrium distance. From this analysis, it is found that $2\pi R\Delta\gamma$ approximates the attractive force at a contacting asperity when the small-scale asperity height is close to atomic equilibrium distance. In Section 6, using this adhesion force of a contacting asperity, an approximated numerical analysis method of rough surface contact between a sphere and a disk combining asperity vdW pressure with vdW forces between mean height planes is presented. The contact characteristics for the 2-mm-radius glass slider and magnetic disk are calculated using asperity parameter values measured in the experiment and compared with experimental ones. It is shown that the overestimated LJ attractive forces yield an adhesion force much smaller than the measured values.

2. Nomenclature

A: Hamaker constant (J)

E^*: Composite Young's modulus of two mating surfaces (Pa)

F_{el}: Elastic contact force of spherical slider (N)

F_{LJ}: Lennard–Jones attractive force (N)

F_{LJa}: Lennard–Jones attractive force due to contacting asperities (N)

F_{ex}: External force applied to disk surface by slider (N)

R: Radius of curvature of spherical slider (m)

R_{a}: Radius of curvature of asperity (m)

O-$r\theta z$, O-$s\varphi z$: Cylindrical coordinate system

P_{el}: Elastic contact pressure (Pa)

P_{ela}: Elastic contact pressure due to contacting asperities (Pa)

P_{LJ}: Lennard–Jones attractive pressure due to mean height planes (Pa)

P_{LJa}: Lennard–Jones attractive pressure due to contacting asperities (Pa)

a: Analytical radius of contact area (m)

$b(r)$: Surface contour of spherical slider (m)

d: Separation of spherical slider from mean height of undeformed disk surface (z-position of tip of spherical slider) (m)

$h(r)$: Spacing between spherical slider and mean height plane of disk surface (m)

h_0: Spacing between tip of spherical slider and mean height plane of disk surface (m)

r_{c}: Contacting radius between spherical slider and disk (m)

$w(r)$: Deformation distribution of disk (m)

$w_{\mathrm{G}}(r)$: Deformation distribution of disk due to a unit force (Green function) (m/N)

z_0: Atomic equilibrium distance (m)

$\Delta\gamma$: Change in total surface energy due to contact (J/m^2)

σ: Spacing between mating mean height planes due to roughness asperities (m)

σ_{a}: rms asperity height (m)

ρ: Asperity density of rough surface (m^{-2})

3. Analytical Model and Numerical Calculation Method

3.1. Analytical Model and Basic Equations

Figure 1 shows the analytical model for asperity contact mechanics analysis of the spherical slider and flat disk treated in this paper. Since the geometries of the sphere and the disk are axisymmetrical, cylindrical coordinate system O-$r\theta z$, (O-$s\varphi z$) is fixed on the mean height plane of the original disk surface without considering deformation. The radius of the spherical slider is denoted by R. The z-position of the tip of the spherical slider is denoted by d, defined as separation. As is common in asperity contact mechanics, elastic and surface roughness properties of the spherical slider are included in those of the disk, and the slider is assumed as a smooth, rigid sphere. The disk has a composite Young's modulus and a composite roughness. It

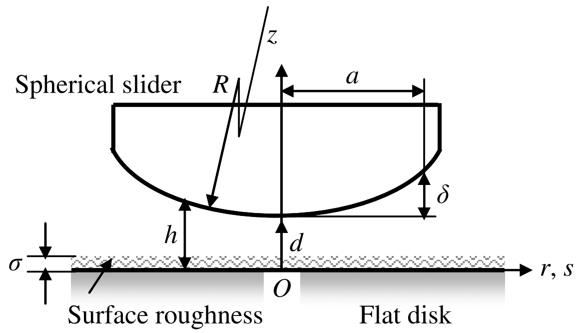

Figure 1. Analytical model of a spherical slider and a flat disk.

is assumed that the mating mean height planes are separated by σ in the contact region after asperity is compressed due to contacting force.

If we denote the observed position by (r, θ) and applied force position by (s, φ), disk deformation caused by a unit force is given by the following Green function [21]:

$$w_{\mathrm{G}}(r, s) = \frac{1}{\pi E^* \sqrt{r^2 + s^2 - 2rs\cos(\theta - \varphi)}}. \tag{1}$$

Here, E^* is the composite Young's modulus given by

$$\frac{1}{E^*} = \frac{1 - \nu_1^2}{E_1} + \frac{1 - \nu_2^2}{E_2}, \tag{2}$$

where E_1 and E_2 are Young's moduli, and ν_1 and ν_2 are Poisson's ratios of the disk and the slider, respectively. Lennard–Jones (LJ) pressure acting on the mean height planes with spacing $h(r)$ is given by

$$P_{\mathrm{LJ}}(h) = \frac{A}{6\pi h^3}\left\{1 - \left(\frac{z_0}{h}\right)^6\right\}. \tag{3}$$

Here, A is the Hamaker constant and z_0 is the atomic equilibrium distance [5]. Note that since z_0 is very small compared to the asperity height of the spherical glass slider and magnetic disk, P_{LJ} is almost equal to vdW pressure, ignoring the second term inside the braces. Since the z-position of the tip of the spherical slider is denoted by d, the contour $b(r)$ of the slider surface in the z-direction is written as

$$b(r) = d + \frac{r^2}{2R}. \tag{4}$$

Note that if $d < \sigma$, the slider penetrates into the disk through the asperity contact. If we denote the elastic deformation of the mean height plane of the disk surface by $w(r)$, the spacing $h(r)$ between the slider and disk is given by

$$h(r) = b(r) - w(r). \tag{5}$$

When the slider does not contact the disk, the disk deformation $w(r)$ is given by

$$w(r) = \iint P_{\mathrm{LJ}}(h(s)) w_{\mathrm{G}}(r, s) s \, \mathrm{d}s \, \mathrm{d}(\varphi - \theta). \tag{6}$$

Under a non-contact condition, disk deformation can be determined by simultaneously solving the discretized equations from (1) to (6). Since the spacing $h(r)$ is altered by deformation $w(r)$, a convergent solution can be obtained through iteration process.

3.2. Numerical Analysis Method for Contact Characteristics

When the separation d decreases, the slider comes in contact with asperities on the disk surface. If we denote LJ pressure due to contacting asperities and elastic contact pressure due to contacting asperities by P_{LJa} and P_{ela}, respectively, the disk deformation is written as

$$w(r) = \iint (P_{\mathrm{LJ}} + P_{\mathrm{LJa}} - P_{\mathrm{ela}}) w_{\mathrm{G}}(r, s) s \, \mathrm{d}s \, \mathrm{d}(\varphi - \theta). \tag{7}$$

In this paper, P_{LJa} and P_{ela} are not treated rigorously but are estimated by an approximation method.

As the separation d decreases further, asperity height is decreased due to the increased contact pressure. However, the asperity becomes too hard to be compressed due to the increased rigidity of the asperities and deformation of mean height plane becomes predominant [18]. This compressed asperity height is represented by the asperity spacing σ between the slider and the disk. This asperity spacing σ is still larger than z_0 in almost all actual cases. If we assume that σ is uniform in the contact area, the spacing $h(r)$ can satisfy the following inequality:

$$h(r) = b(r) - w(r) \geqslant \sigma. \tag{8}$$

When asperity density is not large and $\sigma < 1$ nm, P_{LJa} is smaller than P_{LJ}, as will be shown later. Therefore, at first we ignore P_{LJa}; the effect of P_{LJa} will be taken into account in Section 6.

When the mating surfaces come in contact with each other with an asperity spacing σ, P_{ela} is transmitted to the mean height surface resulting in mean surface deformation. Since the disk deformation is caused by the penetration of the rigid spherical surface, it will be reasonable to assume that P_{el} can be given by Hertzian contact pressure associated with mean plane deformation with contact radius of r_{c}, as follows:

$$P_{\mathrm{el}}(r) = p_{\mathrm{m}} \left\{ 1 - \left(\frac{r}{r_{\mathrm{c}}} \right)^2 \right\}^{1/2}, \quad p_{\mathrm{m}} = \frac{2E^* r_{\mathrm{c}}}{\pi R}. \tag{9}$$

Therefore, disk deformation is given by

$$w(r) = \iint (P_{\mathrm{LJ}} - P_{\mathrm{el}}) w_{\mathrm{G}}(r, s) s \, \mathrm{d}s \, \mathrm{d}(\varphi - \theta). \tag{10}$$

The reason for the minus sign on P_{el} is that elastic contact pressure acts in the $-z$ direction. Under the contact condition, a solution that simultaneously satisfies equations (1), (3), (4), (8), (9) and (10) must be obtained.

To perform the integration in equations (6) and (10), w_G was expanded into a Taylor series with respect to $k = 2rs/(r^2 + s^2)$, and then each expanded term was integrated by $d(\varphi - \theta)$ in the circumferential direction. The number of expanded terms sufficient to give a precise solution was examined by solving the Hertzian contact deformation caused by the Hertzian contact pressure, equation (9). Since a precise Hertzian contact deformation can be obtained using 1000 terms, 2000 terms of an expanded Taylor series were used for the calculation of the influence coefficient to save computing time. Integrations in equations (6) and (10) with respect to radial coordinate were performed numerically by expressing the continuous quantity by N representative points along the radial coordinate.

Figure 2 is a flowchart for numerical calculation. First, the initial separation value d is assumed. When $d > \sigma$, equation (6) is solved. Then, whether or not the disk deformation can satisfy the non-contact condition is examined. If the disk and slider do not contact each other, disk deformation and spacing are solved iteratively as a

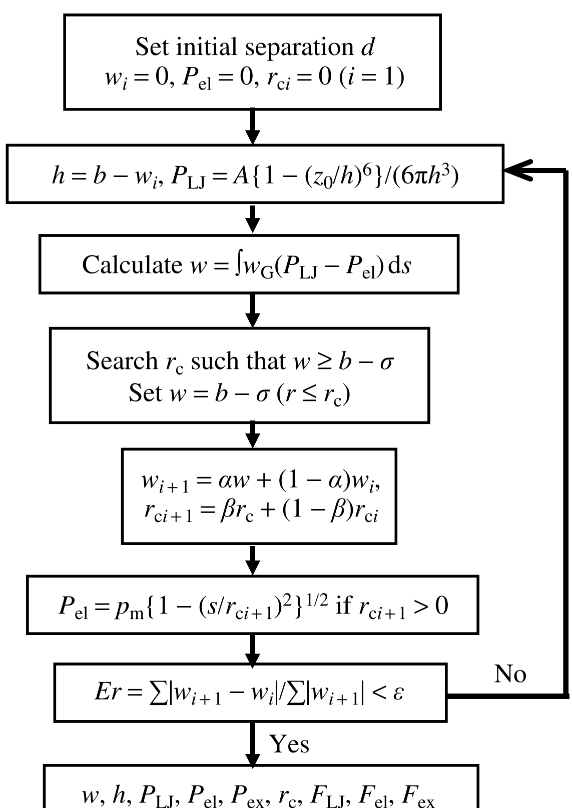

Figure 2. Flowchart for numerical calculation.

non-contact problem using equations (1), (3), (4), (5) and (6). When disk deformation does not satisfy the inequality condition equation (8), the contact area radius r_c that satisfies $w(r_c) = b(r_c) - \sigma$ is numerically calculated, letting the disk deformation w be equal to $b - \sigma$ in the contact region of $r \leqq r_c$. Then, the new disk deformation $w(r)$ is calculated from equations (9) and (10) using the modified disk deformation $w(r)$, spacing $h(r)$, and contact radius r_c. This calculation procedure is repeated until a convergent solution is obtained. The convergence of the solution was determined when the Er value (the ratio of the sum of the absolute values of the differences of the successive values of w_{ij} to the sum of the absolute values of w_{ij}) was less than a small criterion value of ε. The discretized number of the radial coordinate is selected as $N = 400$ although $N = 100$ is enough for calculation of Hertzian contact deformation.

As shown in Fig. 2, in order to avoid the divergence of the solution due to the rapid changes of w and r_c, under-relaxation factors α and β are used for updating deformation w and contact boundary r_c in the iterative calculation. Usually, the criterion of $\varepsilon = 10^{-6}$ was used, but the solution with $Er = {\sim}10^{-2}$ was also considered to be an approximate solution because no clear difference between the solutions with $Er = {\sim}10^{-2}$ and 10^{-6} was observed in the plots of w and r_c.

From the convergent solutions of LJ attractive pressure P_{LJ} and elastic contact pressure P_{el}, LJ attractive force F_{LJ}, elastic contact force F_{el}, and external force applied to disk F_{ex} were calculated by integration of the associated pressures over the analytical area as follows:

$$\text{LJ attractive force} \quad F_{\mathrm{LJ}} = \sum_{1}^{N} P_{\mathrm{LJ}}, \tag{11}$$

$$\text{Elastic contact force} \quad F_{\mathrm{el}} = -\sum_{1}^{M} P_{\mathrm{el}}, \tag{12}$$

$$\text{External force applied to the disk} \quad F_{\mathrm{ex}} = \sum_{1}^{N} (P_{\mathrm{LJ}} - P_{\mathrm{el}}). \tag{13}$$

Since F_{LJ} and F_{ex} are external forces applied to the disk from the slider, the external forces applied to the slider from the disk are given by $-F_{\mathrm{LJ}}$ and $-F_{\mathrm{ex}}$.

4. Calculated Results for Contact Characteristics Ignoring Asperity LJ Forces

The parameter values used for the following calculations are listed in Table 1. These parameter values are the same as those of the 2-mm-radius glass slider and magnetic disk used for the dynamic adhesion force measurements [19, 20]. Accurate values of the Hamaker constant and the atomic equilibrium distance are not known. A Hamaker constant of $A = 10^{-19}$ J was used as a standard value although this

Table 1.
Parameter values used for calculation

Physical parameter	Unit	Value
Disk Young's modulus E_1	GPa	163
Slider Young's modulus E_2	GPa	83
Disk Poisson ratio ν_1		0.3
Slider Poisson ratio ν_2		0.21
Slider radius R	mm	2
Hamaker constant A	J	10^{-19}
Atomic equilibrium distance z_0	nm	0.165

may overestimate the value for the head–disk interface. Equilibrium distance of $z_0 = 0.165$ nm was used since the same value is used as a standard value in the literature by Israelachvili [22] and Mate [23]. However, the effect of repulsive force is negligibly small when $\sigma \geqslant 0.3$ nm. The analytical area radius a was chosen to satisfy δ $(= a^2/2R) = 10$ nm in Fig. 1.

Figure 3 shows the calculated contact characteristics when separation d is decreased from 2 nm to -5 nm in 0.2-nm steps: (a) disk deformation w, (b) LJ attractive pressure P_{LJ}, (c) elastic contact pressure P_{el}, (d) LJ attractive force $-F_{\mathrm{LJ}}$, external force applied to the slider $-F_{\mathrm{ex}}$, and Hertzian contact force F_{el} *versus* separation d, (e) external slider $-F_{\mathrm{ex}}$ force *versus* contact radius r_{c}, and (f) iteration number *IN* and the value of $-10\log(Er)$. In this calculation the criterion of convergence was $\varepsilon = 10^{-6}$. We note from Fig. 3(a) that the disk first deforms upwards ($w > 0$) slightly due to the LJ attractive pressure while d decreases from 2.0 nm to 1.2 nm. But, at $d = 1.0$ nm, the slider comes in contact with disk asperities with a height $\sigma = 1.0$ nm. As d decreases further from 1 nm, the slider penetrates into the disk. The reason P_{LJ} is limited to a constant value at any separation (see Fig. 3(b)) is that spacing $h(r)$ in the contact region is equal to asperity spacing σ. When $\sigma = 1.0$ nm, we note from Fig. 3(b) and 3(c) that P_{LJ} is in the order of MPa, while P_{el} is one order larger than P_{LJ}. Therefore, disk deformation w is close to Hertzian contact deformation. Figure 3(d) shows that $F_{\mathrm{LJ}} = 0.25$ mN at $d = -5$ nm and the minimum value of $-F_{\mathrm{ex}}$ is ~ -0.03 mN at $d = 1.1$ nm. The relationship between contact radius r_{c} and external force F_{ex} is described by the Johnson–Kendall–Roberts (JKR) theory as $r_{\mathrm{c}}^3 = 3R\{(-F_{\mathrm{ex}}) + 3\pi\Delta\gamma R + [6\pi\Delta\gamma R(-F_{\mathrm{ex}}) + (3\pi\Delta\gamma R)2]^{1/2}\})/4E^*$, whereas the relationship is described by the DMT theory as $r_{\mathrm{c}}^3 = 3R\{(-F_{\mathrm{ex}}) + 2\pi\Delta\gamma R\}/4E^*$ [24]. The contact radii given by the JKR and DMT theories are plotted in Fig. 3(e) for comparison using the relationship between $\Delta\gamma$ and A, which will be explained later. The difference between the JKR and DMT theories is small because the LJ attractive force is small and the present numerical results show values almost in between the external forces calculated from the JKR and DMT theories. It is seen

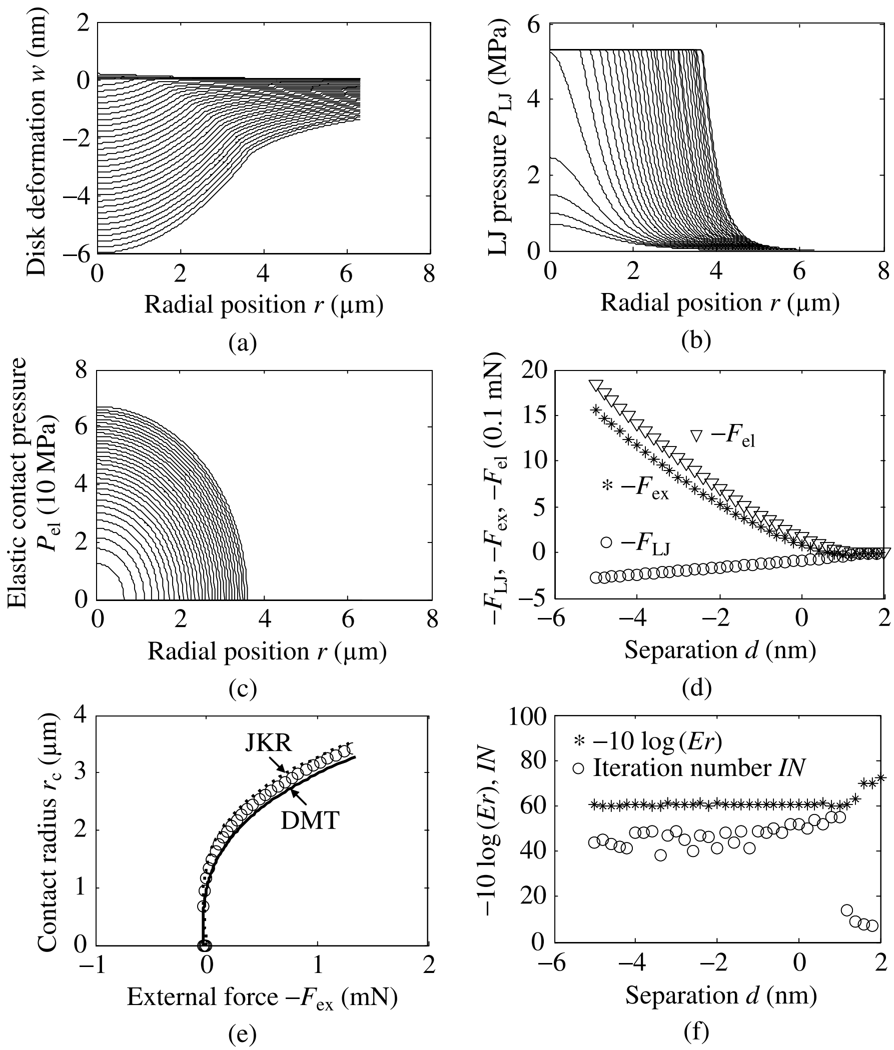

Figure 3. Calculated results for (a) disk deformation $w(r)$, (b) LJ pressure P_{LJ}, (c) elastic contact pressure P_{el}, (d) LJ force $-F_{\mathrm{LJ}}$, external force $-F_{\mathrm{ex}}$, and elastic contact force F_{el} *versus* separation d, (e) contact radius r_{c} *versus* external force $-F_{\mathrm{ex}}$ and (f) iteration number (IN) and numerical error $-\log(Er)$ when d is varied from 2 nm to -5 nm by 0.2 nm ($R = 2$ mm, $\sigma = 1.0$ nm, $\varepsilon = 10^{-6}$).

from Fig. 3(f) that convergent solution with an error of less than 10^{-6} could be obtained with an iteration number of less than 100.

Figure 4 shows similar calculated contact characteristics when $\sigma = 0.5$ nm. The effect of σ on contact characteristics can be seen from a comparison between Figs 3 and 4. As seen in Fig. 4(f), convergence of the solution under contact conditions becomes worse and Er does not decrease to less than $\sim 10^{-2}$ even when the iteration number increases to 200. This is because the contact boundary does not converge to

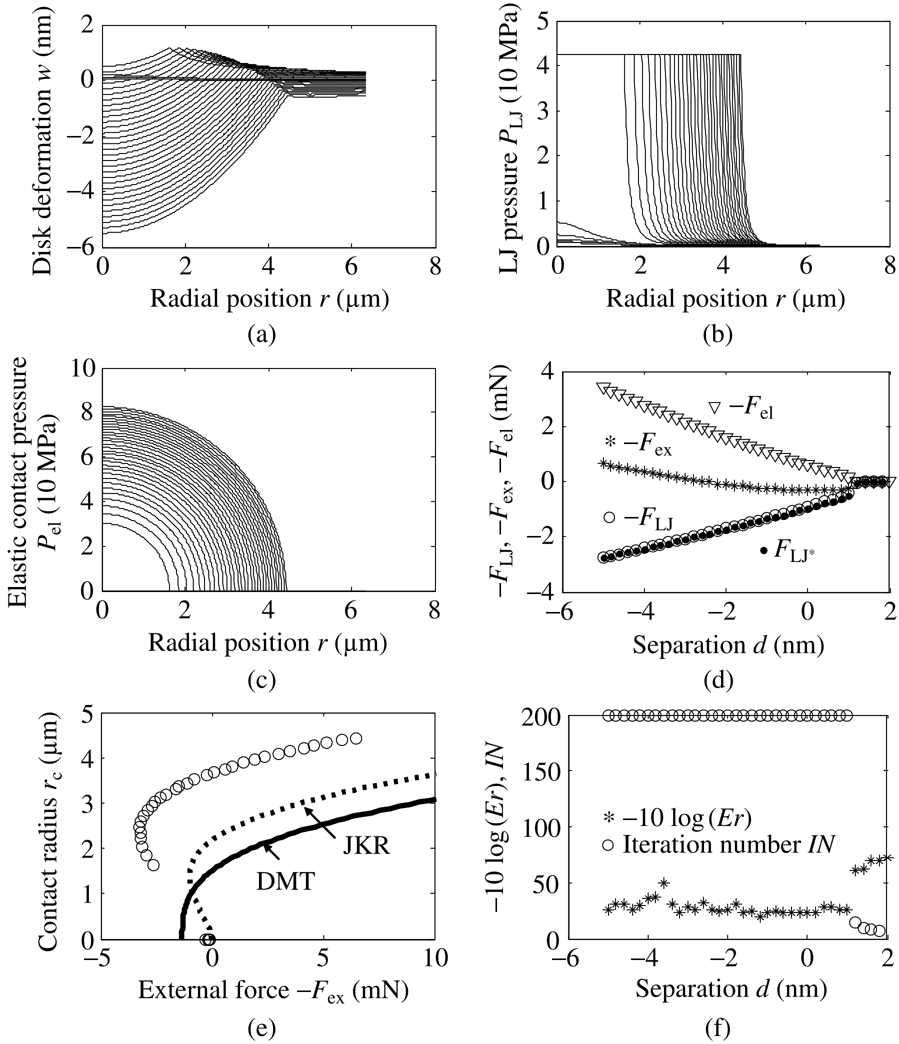

Figure 4. Calculated results for (a) disk deformation $w(r)$, (b) LJ pressure P_{LJ}, (c) elastic contact pressure P_{el}, (d) LJ force $-F_{LJ}$, external force $-F_{ex}$, and elastic contact force F_{el} *versus* separation d, (e) contact radius r_c *versus* external force $-F_{ex}$ and (f) iteration number (*IN*) and numerical error $-\log(Er)$ when d is varied from 2 nm to -5 nm in 0.2 nm steps ($R = 2$ mm, $\sigma = 0.5$ nm, $\varepsilon = 10^{-6}$).

a single value and shows a small cyclic variation. However, even when $Er = 10^{-2}$, variations of not only F_{LJ} and F_{el}, but also of $w(r)$, P_{LJ} and r_c are too small to be visible in the figure. Thus these results are considered to be reliable approximate solutions.

As seen from Fig. 4(a) and 4(d), disk deforms upwards slightly as in the same manner as in Fig. 3(a) while d decreases from 2.0 nm to 1.2 nm. Then, at $d = 1.0$ nm, the disk surface snaps into contact with the slider. It is noted that the disk deformation reaches 1 nm at the periphery of contacting area and that the contact radius abruptly increases as seen in Fig. 4(e). The reason why the contact radius increases appreciably compared to that from JKR theory is not clear, but is considered as follows. Since the spacing between mating mean height planes is equal to asperity height $\sigma = 0.5$ nm, repulsive pressure in equation (3) is almost zero and only elastic contact pressure opposes the attractive pressure in this model. Therefore, the total attractive pressure is stronger than that from the JKR model for a smooth spherical surface, where the effect of repulsive pressure inside the contact area is taken into account. Since P_{LJ} in Fig. 4(b) is 10 times larger than that in Fig. 3(b) and becomes comparable with P_{el} in Fig. 4(c) when $h = \sigma = 0.5$ nm, the disk adheres to the slider at the beginning of contact resulting in a large contact radius even at $d = 0.5$–1.0 nm. Note that the Tabor's parameter value of μ $(= (R\Delta\gamma^2/E^{*2}/z_0^3)^{1/3})$ is 1.64 in this case. The minimum value of $-F_{\mathrm{ex}}$ is about -0.3 mN, and $r_{\mathrm{c}} = 3.7$ μm at $F_{\mathrm{ex}} = 0$, as seen from Fig. 4(e).

As seen in Fig. 4(d), as d is decreased, $-F_{\mathrm{ex}}$ first decreases slightly and then decreases abruptly because the disk adheres to the slider at $d = \sim 1.0$ nm. After reaching the minimum value, $-F_{\mathrm{ex}}$ increases due to the increase in elastic contact force, as seen in Fig. 4(d) and 4(e). Although Fig. 4 shows the calculated results in the approach process, almost the same characteristics without a visible hysteresis were obtained in the separation process when d was increased reversely.

Figure 5(a) and 5(b) shows the LJ attractive force F_{LJ} as a function of the minimum spacing $h_0 = b(0) - w(0)$ at the tip of the spherical slider for $\sigma = 1.0$ and 0.5 nm, respectively. For comparison, the vdW force of F_{vr} $(= AR/6h_0^2)$ between a rigid sphere and a flat disk and the meniscus force of $F_{\mathrm{m}} = 4\pi R\gamma$ ($\gamma = 0.022$ J/m^2) are shown in these figures. Noting that the separation d is decreased from 2 to -5 nm in 0.2-nm steps, h_0 is slightly smaller than d due to the elastic deformation under non-contact conditions. However, F_{LJ} is almost equal to F_{vr} at the same h_0 under the non-contact conditions. This indicates that the attractive pressure in a small area of the protruded tip of the sphere contributes to the total attractive

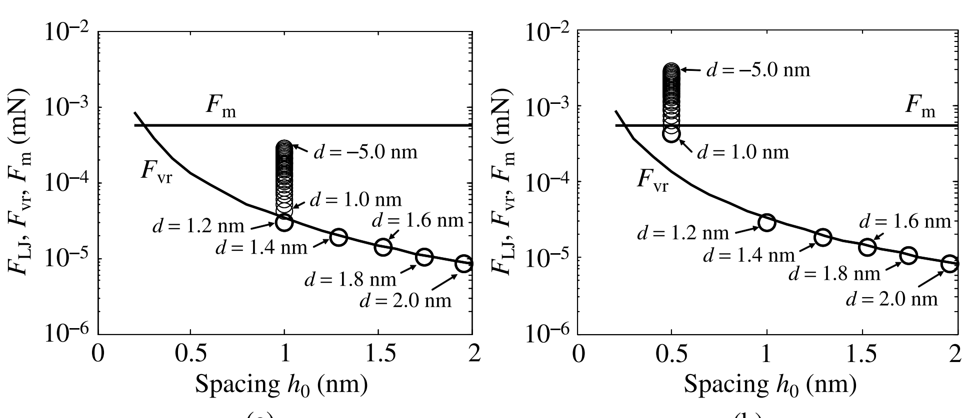

Figure 5. F_{LJ} (○), F_{vr} and F_{m} *versus* h_0 for (a) $\sigma = 1.0$ nm and (b) $\sigma = 0.5$ nm.

force. When h_0 decreases to less than 1.0 nm, the disk snaps into contact with the slider and h_0 jumps to σ. Therefore, no jump is observed when $\sigma = 1.0$ nm, but a clear jump of h_0 from 1.0 nm to 0.5 nm ($=\sigma$) is observed at $d = 1.0$ nm when $\sigma = 0.5$ nm. F_{LJ} jumps from the curve of F_{vr} to a value much larger than F_{vr} because of increase in contact area. F_{LJ} becomes larger than the meniscus force F_{m} when $d < 0.6$ nm.

The adhesion force at h_0 under contact conditions is approximately evaluated by summing the LJ force of rigid sphere contact F_{LJr} at h_0 ($=\sigma$) and the LJ attractive force within the contact area. F_{LJr}, including the repulsive term, is obtained by integrating P_{LJ} in equation (3) over the total surface and written as

$$F_{\mathrm{LJr}} = \frac{AR}{6h_0^2}\left(1 - \frac{z_0^6}{4h_0^6}\right). \tag{14}$$

When $z_0/h_0 < 0.5$, the second term within braces can be neglected and $F_{\mathrm{LJr}} = F_{\mathrm{vr}}$. The LJ attractive force within the contact area can be obtained by multiplying the contact area πr_{c}^2 with $P_{\mathrm{LJ}}(h_0)$. Thus the adhesion force under contact conditions is approximated by

$$F_{\mathrm{LJ}^*} = \frac{AR}{6h_0^2}\left(1 - \frac{z_0^6}{4h_0^6}\right) + \frac{Ar_{\mathrm{c}}^2}{6h_0^3}\left(1 - \frac{z_0^6}{h_0^6}\right). \tag{15}$$

Here the repulsive term can be ignored when $z_0/h_0 < 0.5$. Using the calculated value of r_{c} and $h_0 = \sigma$, $-F_{\mathrm{LJ}^*}$ was calculated and plotted in Fig. 4(d) with a dot. It is clear that F_{LJ^*} agrees well with F_{LJ}.

To take into account the LJ force at contacting asperities, contact characteristics between a small sphere and a flat are calculated next to make clear how the attractive force at contacting asperities is properly evaluated.

5. Evaluation of LJ Attractive Pressure at Contacting Asperities

5.1. LJ Attractive Force between a 1-μm-Radius Sphere and a Flat

In actual cases where asperity density is large and asperity spacing σ is more than 0.5 nm, adhesion characteristics cannot be evaluated well without taking into account the LJ attractive force of contacting asperities. Since an actual rough surface has fractal characteristics, it is natural to consider that an asperity has small-scale asperities whose asperity spacing is of the same order as z_0. If we focus on the smoothest engineering surfaces, such as a magnetic disk, head slider, and silicon substrate, the rms values of surface roughness are less than 0.5 nm and the mean asperity radius is near 1 μm. Therefore, the contact characteristics of a 1-μm-radius asperity with a flat were numerically calculated for various values of asperity spacing and the expression for the asperity attractive force was examined. The analytical model of asperity contact is similar to that shown in Fig. 1.

Figure 6 shows the calculated contact characteristics for $\sigma = 0.25, 0.20, 0.18, 0.165, 0.16$ and 0.15 nm when separation d decreases from 0.6 to -0.5 nm in steps

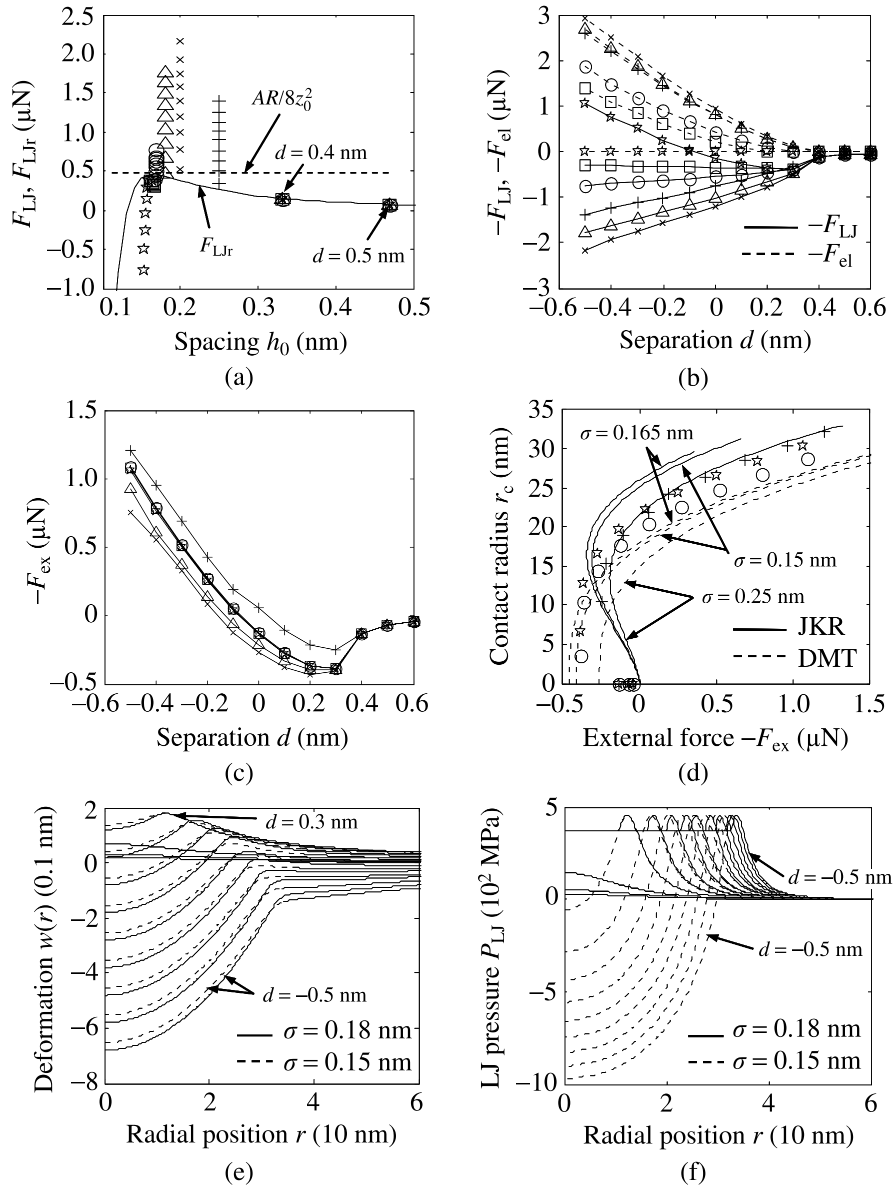

Figure 6. Contact characteristics of 1-μm-radius sphere and disk for $\sigma = 0.25, 0.20, 0.18, 0.165, 0.16$ and 0.15 nm (+: $\sigma = 0.25$ nm, ×: $\sigma = 0.20$ nm, △: $\sigma = 0.18$ nm, ○: $\sigma = 0.165$ nm, □: $\sigma = 0.16$ nm, ☆: $\sigma = 0.15$ nm). (a) F_{LJ} and F_{LJr} *versus* h_0. (b) LJ force $-F_{LJ}$ and elastic contact force F_{el} *versus* separation d. (c) External force $-F_{ex}$ *versus* separation d. (d) Contact radius r_c *versus* external force $-F_{ex}$. (e) Disk deformation $w(r)$. (f) LJ pressure P_{LJ}.

of 0.1 nm: (a) F_{LJ} *versus* h_0, (b) $-F_{LJ}$ and $-F_{el}$ *versus* d, (c) $-F_{ex}$ *versus* d, (d) r_c *versus* $-F_{ex}$, (e) disk deformation w, and (f) LJ pressure P_{LJ}. Figure 6(a) is similar to Fig. 5 but drawn in a linear scale diagram. In Fig. 6(a), the LJ force F_{LJr} for a rigid sphere–flat interface given by equation (14) is plotted with a solid line for comparison. The maximum attractive value, indicated with a dashed line, is given by $F_{\mathrm{LJr\,max}} = AR/8z_0^2$. It is noted from Fig. 6(a) that F_{LJ} increases with decrease in h_0 along the curve of F_{LJr} in non-contact conditions. But after the contact at $h_0 = \sigma$, F_{LJ} increases from F_{LJr} with decrease in d because of the increase in the contact area when $\sigma > 0.16$ nm. In particular, when $\sigma = 0.2$ nm, the F_{LJ} increases to more than 2 μN at $d = -0.5$ nm, which is four times larger than the $F_{\mathrm{LJr\,max}}$. The increase of F_{LJ} with a decrease in d is largest when $\sigma = 0.2$ nm. This is because P_{LJ} inside the contact area, given by equation (3), becomes maximum at $h = \sigma = 3^{1/6}z_0 = 0.198$ nm. Therefore, if the small-scale asperity on a roughness asperity is larger than z_0, attractive force at the contacting asperity should be considered as a function of separation d.

However, if σ is nearly equal to z_0, F_{LJ} has an almost constant value of $AR/8z_0^2$ at any separation as shown in Fig. 6(a) and 6(b). This is because vdW attractive pressure inside the contact area is cancelled by the repulsive pressure and the total attractive force is generated only from the attractive pressure in the surrounding area. This result can also be derived from F_{LJ^*} in equation (15), by substituting $h_0 = z_0$, the attractive force inside the contact area vanishes and the attractive force outside the contact area becomes $AR/8z_0^2$.

When $\sigma = 0.15$ nm (☆), however, F_{LJ} decreases rapidly with decrease in d after contact due to repulsive pressure effect as shown in Fig. 6(a) and 6(b). In this case, sphere and flat do not contact each other, Thus F_{el} is always zero, and $F_{\mathrm{LJ}} = F_{\mathrm{ex}}$, as seen from comparison between Fig. 6(b) and 6(c).

It is noted from Fig. 6(c) that the relationship of F_{ex} ($= F_{\mathrm{H}} - F_{\mathrm{LJ}}$) *versus* d is hardly influenced by σ. Particularly, $-F_{\mathrm{ex}}$ *versus* d is almost identical when $\sigma \leqq z_0$. This indicates that a variation of F_{LJ} due to σ is compensated with a reversal variation of F_{el}, as seen in Fig. 6(b).

In Fig. 6(d), the relationship between contact radius r_{c} and external force $-F_{\mathrm{ex}}$ is compared with those from JKR and DMT theories for three cases of $\sigma = 0.25$ (+), 0.165 (○) and 0.15 (☆) nm. It is observed that the calculated results of r_{c} are close to JKR curve when $\sigma = 0.25$ nm, and are in between JKR and DMT curves when $\sigma = 0.15$ nm. However, the numerical results of r_{c} become closer to DMT curve when $\sigma = 0.165$ nm. This is because the total LJ force F_{LJ} is attributable to LJ pressure outside the contact area as in the DMT model when $\sigma = {\sim}z_0$ as stated above.

Typical disk deformation $w(r)$ and LJ pressure $P_{\mathrm{LJ}}(r)$ are illustrated for $\sigma = 0.18$ and 0.15 nm in Fig. 6(e) and 6(f), respectively when d is changed from 0.6 nm to -0.5 nm in steps of 0.1 nm. Although the disk deformation is changed only slightly by the change of σ, P_{LJ} changes significantly with the change of σ after the disk surface comes in contact with slider ($d \leqq 0.3$ nm). When $\sigma = 0.18$ nm, the disk surface contacts the spherical slider with a spacing of $h_0 = 0.18$ nm. Therefore, P_{LJ} inside the contact area becomes smaller than P_{LJ} in the surrounding area; P_{LJ} becomes maximum at $h = 0.198$ nm as explained above. When $\sigma = 0.15$ nm, the disk surface does not contact the slider because the spacing between the disk and the slider is larger than asperity height σ and the external force F_{ex} becomes equal to F_{LJ}.

Accordingly, it can be said that if and only if the small-scale asperity height is nearly equal to z_0, F_{LJ} at a contacting asperity can be expressed approximately as $AR/8z_0^2$ at any separation. If σ is a little larger than z_0, F_{LJ} at a contacting asperity would increase as separation decreases, as seen in Fig. 6(a) and 6(b). However, if we evaluate the largest adhesion force that can be observed in F_{ex} at the beginning and end of asperity contact, the LJ attractive force can be approximated by $AR/8z_0^2$ when $\sigma \leqq 0.25$ nm. Moreover, as seen from Fig. 6(c), it is expected that the external force $-F_{\mathrm{ex}}$ calculated from $F_{\mathrm{LJ}} = AR/8z_0^2$ for the case of $\sigma = \sim z_0$ can be used for a wider range of σ.

On the other hand, using Derjaguin approximation, the attractive force of a sphere–flat contact has been derived from surface energy and given by

$$F_{\mathrm{a}} = 2\pi R\Delta\gamma, \quad \Delta\gamma = \gamma_1 + \gamma_2 - \gamma_{12}, \tag{16}$$

where γ_1 and γ_2 are surface energies of the mating surfaces 1 and 2 before contact, and γ_{12} is that of the contacting surfaces after the contact. Since F_{a} should be equal to F_{LJr} in equation (14), we can obtain the general relationship between the Hamaker constant A and the surface energy difference $\Delta\gamma$ as follows:

$$\Delta\gamma = \frac{A}{12\pi\sigma^2}\left(1 - \frac{z_0^6}{4\sigma^6}\right), \tag{17}$$

where σ is the effective mean height of small-scale roughness.

When $\sigma \geqslant 1.16z_0$ ($= 0.19$ nm), the second term is less than 0.1. Thus, if the surface energy is determined by the pull-off force of sphere–disk contact that is affected by small-scale roughness, the Hamaker constant is approximately given by

$$A = 12\pi\sigma^2\Delta\gamma. \tag{18}$$

When $\sigma \leqslant 1.04z_0$ ($= 0.172$ nm), and the surface energy is determined from the pull-off force of sphere–flat contact, the Hamaker constant can be given by

$$A = 16\pi z_0^2\Delta\gamma. \tag{19}$$

When the surface energy is determined from the contact angles of liquids, the liquid molecules are considered to contact the solid surface at equilibrium distance. Thus, in this case, equation (19) can be used for the relationship between the surface energy difference and the Hamaker constant. The plotted curves of the JKR and DMT theories illustrated in Figs 3, 4 and 6 were calculated using equation (17).

5.2. Comparison between Asperity LJ Pressure P_{LJa} and Mean Height Plane LJ Pressure P_{LJ}

Next we consider the magnitude of averaged LJ pressure P_{LJa} due to contacting asperities and compare it with the LJ pressure P_{LJ} due to mean height planes. According to the calculated results described above, if the small-scale asperity spacing

σ is close to z_0, the LJ attractive force is given by $AR/8z_0^2$ at $h_0 = z_0$. This maximum attractive force is considered to be equal to F_a in equation (16) with surface energy determined from contact angles of test liquids. In this condition, P_{LJa} is given by

$$P_{LJa} = 2\pi R_a \Delta\gamma \rho p, \tag{20}$$

where R_a, ρ and p are mean asperity radius, asperity density, and probability of contacting asperity out of the entire asperity density ρ.

Since the probability of asperities contacting each other is usually less than 0.5 at separation d at which the minimum external force is observed, it can be said that P_{LJ} plays a dominant role if P_{LJa} at $p = 1.0$ is smaller than P_{LJ} given by equation (3), i.e.,

$$2\pi R_a \Delta\gamma \rho \leqslant \frac{A}{6\pi\sigma^3}\left\{1 - \left(\frac{z_0}{\sigma}\right)^6\right\}. \tag{21}$$

Since σ in inequality (21) is a large-scale asperity spacing, $(z_0/\sigma)^6 \ll 1$. In contrast, since the small-scale asperity spacing can be considered to be nearly equal to z_0, equation (19) holds. Therefore, by substituting equation (19) into inequality (21), we can obtain the condition where P_{LJ} plays a dominant role in attractive pressure compared to P_{LJa}, as follows:

$$\sigma \leqslant \left(\frac{4}{3}\frac{z_0^2}{\pi R_a \rho}\right)^{1/3}. \tag{22}$$

If we assume that $R_a = 1$ µm, then $\sigma \leqslant 1.05$ nm and $\sigma \leqslant 0.49$ nm for $\rho = 10$ and 100 µm^{-2}, respectively. Therefore, when the spacing σ of contacting asperities is less than 0.5 nm, the contact characteristics can be approximately analyzed by ignoring the LJ attractive force of contacting asperities and the contact mechanics analysis in Section 4 can be supported.

6. Calculation of Attractive Force of 2-mm Glass Slider Including Asperity LJ Pressure Effect

If asperity spacing σ is regarded as uniform in the contact area, contact characteristics including LJ pressure due to contacting asperities and mean height planes can be calculated from equation (7) in the same manner as equation (10) using P_{LJa} from equation (20). Ono and Nakagawa [20] measured the dynamic external force when 1- and 2-mm-radius glass spheres bounced on a magnetic disk with a thin lubricant layer. In experiments with a 2-mm smooth glass slider, a maximum attractive force of about 0.4–0.6 mN was detected at the end of the contact period of about 30 µs. To test our belief that the meniscus could be generated so rapidly and that the measured attractive force must, therefore, be a meniscus force, the maximum possible LJ attractive force was calculated by an approximated numerical analysis.

Before calculating eqaution (7), the statistical asperity contact characteristics of two flat rough surfaces, including the asperity LJ pressure P_{LJa} of equation (20), were first calculated following the conventional method similar to [9–11]. In this analysis, however, P_{LJa} was calculated from the attractive forces of contacting asperities given by equation (16). In contrast to the prior method, attractive pressure from noncontacting asperities was taken into account in the mean height plane LJ pressure P_{LJ}.

If we denote asperity height by z, mean asperity height by z_{m}, and asperity height distribution density function by $\phi(z - z_{\mathrm{m}})$ in the z-coordinate shown in Fig. 1, asperity elastic contact pressure P_{ela}, asperity LJ pressure P_{LJa} and real contact area ratio AR_{a} are, respectively, given by

$$P_{\mathrm{ela}} = \frac{4}{3} E^* \rho R_{\mathrm{a}}^{1/2} \int_d^\infty (z - d)^{3/2} \phi(z)\,\mathrm{d}z, \tag{23}$$

$$P_{\mathrm{LJa}} = 2\pi R_{\mathrm{a}} \Delta\gamma \rho \int_d^\infty \phi(z)\,\mathrm{d}z, \tag{24}$$

$$AR_{\mathrm{a}} = \pi R_{\mathrm{a}} \rho \int_d^\infty (z - d)\phi(z)\,\mathrm{d}z. \tag{25}$$

Here, it is assumed that the asperity height has a Gaussian asperity height distribution with rms asperity height σ_{a} and mean asperity height z_{m} of the form:

$$\phi(z) = \frac{1}{\sqrt{2\pi}\sigma_{\mathrm{a}}} \exp\left(-\frac{(z - z_{\mathrm{m}})^2}{2\sigma_{\mathrm{a}}^2}\right). \tag{26}$$

Table 2 lists the surface roughness parameters for the 2-mm-radius glass slider and magnetic disk tested [20]. From Table 2, composite rms asperity height is $\sigma_{\mathrm{a}} = (\sigma_{\mathrm{a1}}^2 + \sigma_{\mathrm{a2}}^2)^{0.5} = (0.15^2 + 0.31^2)^{0.5} = 0.344$ nm, and composite mean asperity height z_{m} is 0.56 nm + 0.52 nm = 1.08 nm. The composite asperity radius is given by $R_{\mathrm{a}} = (R_{\mathrm{a1}}^{-1} + R_{\mathrm{a2}}^{-1})^{-1} = (1.36^{-1} + 3.06^{-1})^{-1} = 0.94$ μm. Since it is not easy to evaluate the equivalent asperity density and probability of asperity contact, various values of ρ were used for numerical calculation.

Table 2.
Surface roughness of the hemispherical R2 glass slider (scan area = 1 μm × 1 μm) and magnetic disk (scan area = 5 μm × 5 μm)

	Roughness			Asperity			
	R_{a} (nm)	R_{q} (rms) (nm)	R_{p} (nm)	Rms height (nm)	Mean height (nm)	Density (μm^{-2})	Mean radius (μm)
R2 slider	0.34	0.33	1.62	0.15	0.56	179	1.36
Disk	0.52	0.67	5.60	0.31	0.52	31.3	3.06

Figure 7 shows the calculated asperity contact characteristics between the flat glass slider and magnetic disk: (a) probability density function $\phi(z)$ and probability p of asperity contact as a function of normalized asperity height $(z - z_m)/\sigma_a$, (b) elastic contact pressure P_{ela} and LJ attractive pressure P_{LJa} *versus* normalized separation $(d - z_m)/\sigma_a$, (c) real contact area ratio *versus* $(d - z_m)/\sigma_a$, and (d) external pressure P_{exa} $(= P_{ela} - P_{LJa})$ *versus* $(d - z_m)/\sigma_a$. Material parameters of the two mating surfaces are as listed in Table 1. Surface energy $\Delta\gamma$ is assumed to be 0.06 J/m^2 ($A = 0.821 \times 10^{-20}$ J from equation (19)). The effect of asperity density ρ on contact characteristics is shown in Fig. 7.

As seen in Fig. 7(b) and 7(d), the external pressure P_{exa} has a minimum negative value at $(d - z_m)/\sigma_a = \sim 1$ and becomes positive when $(d - z_m)/\sigma_a < 0$. Figure 7(a) and 7(c) shows that the real contact area ratios are 0.013, 0.04 and 0.073 for $\rho =$ 31.3, 100 and 179 μm^{-2}, respectively, at 50% probability of asperity contact. Since

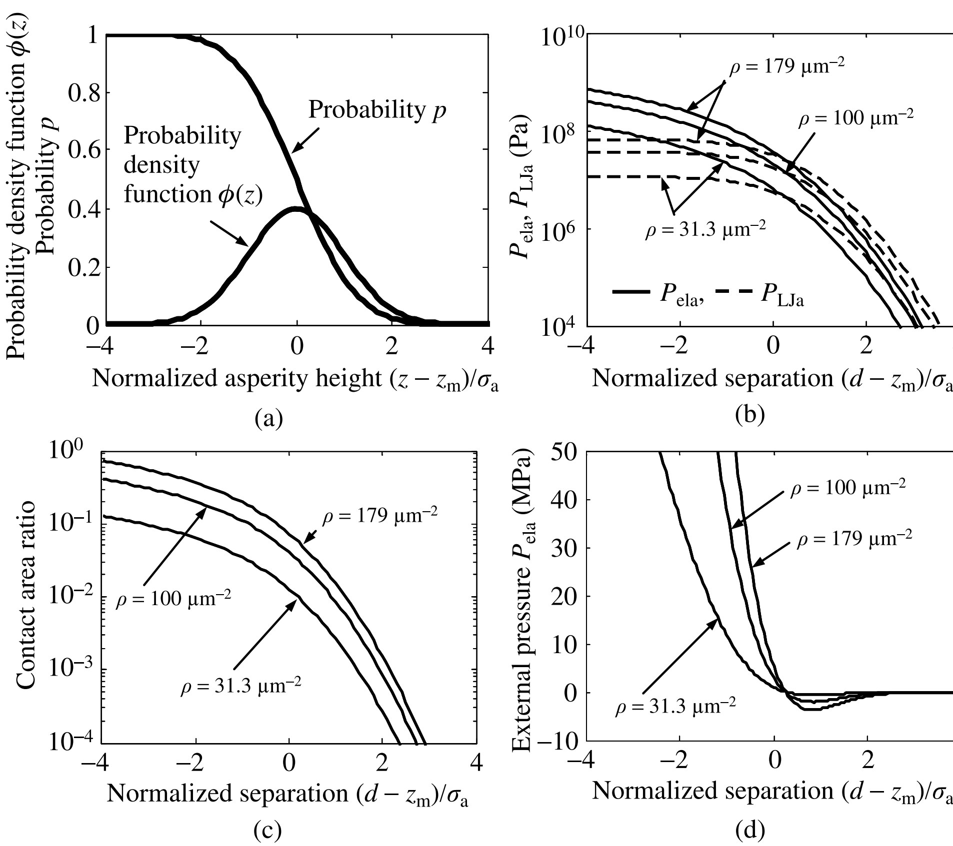

Figure 7. Statistical asperity contact characteristics of a flat rough surface with Gaussian asperity height distribution. (a) Probability density function $\phi(z)$ and probability p of contacting asperities *versus* normalized asperity height $(z - z_m)/\sigma_a$. (b) Asperity contact pressure P_{ela} (solid) and asperity LJ pressure P_{LJa} (dashed) *versus* normalized separation $(d - z_m)/\sigma_a$. (c) Real contact area ratio *versus* $(d - z_m)/\sigma_a$. (d) External pressure $P_{exa}(= P_{ela} - P_{LJa})$ *versus* $(d - z_m)/\sigma_a$.

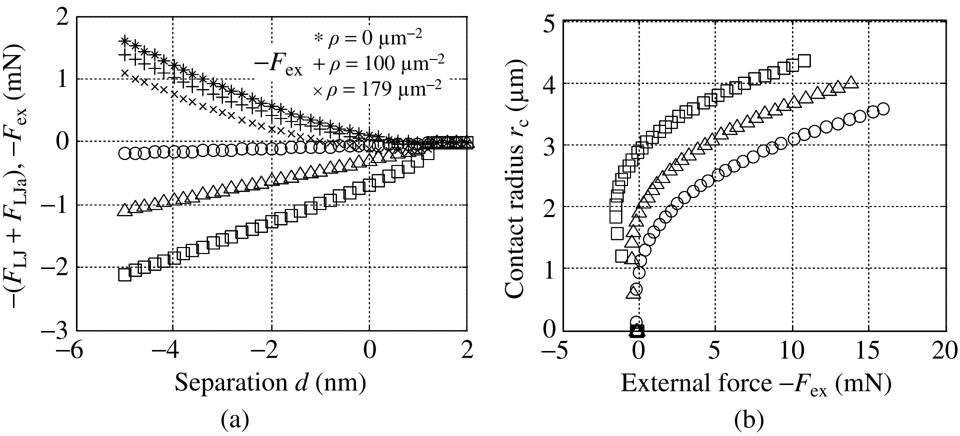

Figure 8. Contact characteristics of 2-mm-radius glass slider and magnetic disk including the effect of LJ pressures due to contacting asperities and mean height planes (○: $\rho = 0\ \mu m^{-2}$, △: $\rho = 100\ \mu m^{-2}$, □: $\rho = 179\ \mu m^{-2}$). (a) LJ force $-(F_{LJ} + F_{LJa})$ and external force $-F_{ex}$ applied to the slider *versus* separation d. (b) Contact radius r_c *versus* external force $-F_{ex}$.

the real contact area ratio at $\rho = 179\ \mu m^{-2}$ increases to 0.55 at $(d - z_m)/\sigma_a = -3$, it seems that an asperity density of 179 would be an overestimated value. Since we are interested in the region of negative external pressure, 50% probability of asperity contact would be sufficient for estimating the asperity attractive force.

Therefore, for the calculation of equation (7), it is reasonable to consider that the contact asperity spacing σ is $\sim z_m$ (= 1.08 nm) and probability of contacting asperities p is ~0.5. When $p = 0.5$, P_{LJa} values in equation (20) become 5.56, 17.7 and 31.8 MPa for $\rho = 31.3$, 100 and 179 μm^{-2}, respectively. These asperity LJ pressures were used to calculate asperity contact characteristics with equations (7), (8) and (9).

Figure 8 shows (a) $-(F_{LJ} + F_{LJa})$ and $-F_{ex}$ $(= -F_{LJ} - F_{LJa} + F_{ela})$ *versus* separation d and (b) r_c *versus* $-F_{ex}$ for asperity densities of $\rho = 0$, 100 and 179 μm^{-2}. These solutions have an accuracy of $\varepsilon = 10^{-6}$. As seen in Fig. 8(a), the total attractive force $-(F_{LJ} + F_{LJa})$ increases with an increase in asperity density and with a decrease in d, but the minimum negative value of $-F_{ex}$ is not appreciable. In Fig. 8(b), the minimum values of $-F_{ex}$ are 0.022, 0.05 and 0.151 mN for $\rho = 0$, 100 and 179 μm^{-2}, respectively.

Figure 9 shows a comparison between the experimental dynamic indentation characteristics presented in a previous paper [20] and the calculated external force applied to the slider. The experimental relationship between force applied to the slider and displacement was calculated by differentiation and integration of the slider velocity in the bouncing process that was measured by a digital laser Doppler vibrometer. Experimental results show a small adhesion force at the beginning of the contact and a large adhesion force of −0.4 to −0.6 mN at the end of the contact. It should be noted that these force–displacement characteristics of the slider were

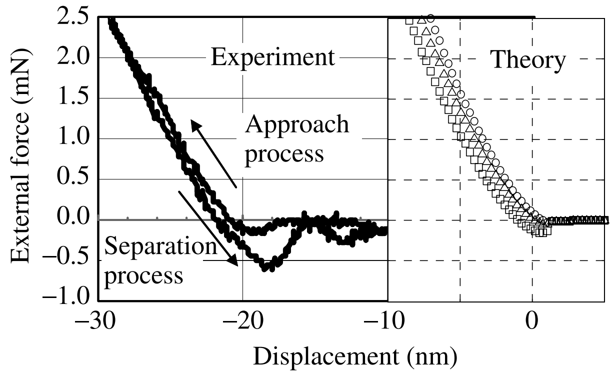

Figure 9. Comparison between experimental and theoretical indentation characteristics. Experimental results: lubricant thickness = 2 nm, mobile lubricant thickness = 0.98 nm, and impact velocity = 0.75 mm/s. Theoretical results: ○ $\rho = 0\ \mu m^{-2}$ ($P_{LJa} = 0$ MPa), △ $\rho = 100\ \mu m^{-2}$ ($P_{LJa} = 17.7$ MPa), and □ $\rho = 179\ \mu m^{-2}$ ($P_{LJa} = 31.8$ MPa).

measured for only 30 μs contact time with magnetic disk with a mobile lubricant thickness of 0.98 nm. In the numerical calculation, the difference between approach and separation processes was too small to be visible in the figure. The calculated adhesion force is about 0.15 mN even when $\rho = 179\ \mu m^{-2}$. Therefore, the small adhesion force experimentally observed at the beginning of the contact might be caused by LJ adhesion force. However, the large adhesion force observed at the end of the contact is not caused by LJ attractive pressure. The meniscus force of lubricant with surface energy γ is given by $2\pi R\gamma(1 + \cos\theta_0)$ where θ_0 is the contact angle of lubricant on the glass slider and γ is the surface energy of the lubricant. Since $\gamma = 0.022$ J/m^2 in the experiment, the meniscus force $4\pi R\gamma$ is 0.55 mN when $\theta_0 = 0$ degrees. Therefore, it is natural to consider that the adhesion force observed at the end of the contact is caused by meniscus formation within a short contact period of 30 μs.

7. Conclusion

A numerical analysis method is presented for the rough surface contact characteristics between a sphere and a disk considering not only elastic deformation and LJ forces between mean height planes of the sphere and disk but also LJ forces of contacting asperities, and the intermolecular force between the glass slider and the magnetic disk is evaluated. The effects of LJ forces of contacting asperities and their elastic deformation and elastic contact force are taken into account. Fundamental contact characteristics of a 2-mm-radius glass sphere and a 1-μm-radius asperity model on the glass slider were calculated by assuming asperity spacing due to different scale asperity heights. The relationship between the Hamaker constant and the surface energy is discussed. This analysis suggests that LJ attractive force at a contacting asperity is given by $2\pi R\Delta\gamma$ at any separation if the spacing between the contacting asperity and the mating surface is close to atomic equilibrium distance. By using this adhesion force for contacting asperities, an approximate numerical analysis method for rough-surface contact between a sphere and a flat disk, including elastic deformation and LJ pressures of contacting asperities and mean height planes, is presented. The contact characteristics for the 2-mm-radius glass slider and magnetic disk are calculated using asperity parameters measured in the experiment and compared with experimental adhesion force values. It is shown that the calculated adhesion force is much smaller than the measured adhesion force, supporting the idea that the adhesion force measured at the end of the contact is generated from meniscus force rather than from vdW force.

References

1. K. L. Johnson, K. Kendall and A. D. Roberts, *Proc. R. Soc. Lond. Ser. A* **324**, 301–313 (1971).
2. B. V. Derjaguin, V. M. Muller and Y. P. Toporov, *J. Colloid Interface Sci.* **53**, 314–326 (1975).
3. M. D. Pashley, *Colloids Surfaces* **12**, 69–77 (1984).
4. D. Maugis, *J. Colloid Interface Sci.* **150**, 243–269 (1992).
5. P. Attard and J. L. Parker, *Phys. Rev. A* **46**, 7959–7971 (1992).
6. J. A. Greenwood, *Proc. R. Soc. Lond. Ser. A* **453**, 1277–1297 (1997).
7. J. Q. Feng, *Colloids Surfaces* **172**, 175–198 (2000).
8. J. A. Greenwood and J. B. P. Williamson, *Proc. Roy. Soc. (London)* **A295**, 300–319 (1966).
9. W. R. Chang, I. Etsion and D. B. Bogy, *ASME Trans. J. Tribology* **110**, 50–56 (1988).
10. H. M. Stanley, I. Etsion and D. B. Bogy, *ASME Trans. J. Tribology* **112**, 98–104 (1990).
11. A. Y. Suh and A. A. Polycarpou, *J. Appl. Phys.* **99**, 104328 (2005).
12. N. Yu and A. A. Polycarpou, *J. Colloid Interface Sci.* **278**, 428–435 (2004).
13. A. R. Ambekar, V. Gupta and D. B. Bogy, *ASME Trans. J. Tribology* **127**, 530–536 (2005).
14. S.-C. Lee and A. A. Polycarpou, *ASME Trans. J. Tribology* **126**, 334–341 (2004).
15. H. Matsuoka, S. Ohkubo and S. Fukui, *Microsys. Technol.* **11**, 824–829 (2005).
16. K. Ono and M. Yamane, *ASME Trans. J. Tribology* **129**, 65–74 (2007).
17. K. Ono and M. Yamane, *ASME Trans. J. Tribology* **129**, 246–255 (2007).
18. K. Ono and Y. Masami, *ASME Trans. J. Tribology* **129**, 453–460 (2007).
19. K. Ono and K. Nakagawa, *JSME International J. Ser. C* **49**, 1159–1170 (2006).
20. K. Ono and K. Nakagawa, *Tribology Lett.* **31**, 77–89 (2008).
21. K. Ono, *JSME Trans.* **51**, 2309–2316 (1985).
22. J. N. Israelachvili, *Intermolecular and Surface Forces*, 2nd edn, pp. 196–197. Academic Press (1992).
23. C. M. Mate, *Tribology on the Small Scale*, p. 153. Oxford University Press (2008).
24. X. Shi and Y.-P. Zhao, *J. Adhesion Sci. Technol.* **18**, 55–68 (2004).

Equilibrium Vapor Adsorption and Capillary Force: Exact Laplace–Young Equation Solution and Circular Approximation Approaches

D. B. Asay [a,*], **M. P. de Boer** [b,c] **and S. H. Kim** [a,†]

[a] Department of Chemical Engineering, Pennsylvania State University, University Park, PA 16802, USA

[b] Sandia National Laboratories, Albuquerque, NM 87185, USA

[c] Department of Mechanical Engineering, Carnegie Mellon University, Pittsburgh, PA 15237, USA

Abstract

The capillary adhesion force of an asperity of radius R as a function of vapor partial pressure is calculated using exact and approximate methods assuming a continuum model. The equilibrium between the capillary meniscus at the asperity and the adsorbate film on the surface is discussed through a disjoining pressure term. It is found that the two methods agree very well over a wide partial pressure range. Without taking into account the effect of the adsorbate film, the theoretical calculation results do not show the experimental partial pressure dependence of the capillary force except near the saturation vapor condition. The experimental capillary force trend with partial pressure can be explained when the presence of the adsorbate film is included in the calculation.

Keywords

Capillary forces, nanoscale, disjoining pressure, adsorption, equilibrium

1. Introduction

When a liquid meniscus is formed around the contact area of two neighboring surfaces, a force is exerted on the contacting surfaces due to the surface tension of the liquid and the curvature of the meniscus. This is called a capillary force. Capillary forces play important roles in studies of adhesion between particles and particles to flat or curved surfaces, adhesion of insects and small animals, particle processing, friction, etc. Compared to body forces, the relative strength of the capillary force becomes larger as the size of the object decreases, and, unless avoided, immediately leads to the "stiction" problem in microelectromechanical systems (MEMS).

---

* Current address: PPG, Allison Park, PA 15101, USA.

† To whom correspondence should be addressed. E-mail: shkim@engr.psu.edu

Even if the partial pressure of the vapor in the ambient is lower than its saturation pressure, a condensed phase can be formed in the narrow gap of two solid surfaces if the vapor molecule has a strong affinity toward the solid surface. This phenomenon is called capillary condensation and is explained well by the equilibrium relationship between the Laplace pressure due to the curvature of the condensed liquid meniscus and the vapor pressure (see Section 2.1). Alcohol vapors have been shown to be highly efficient to prevent MEMS failure compared to other coating based lubrication approaches [1–3], but are expected to form capillaries of the condensed liquid at the asperity contacts depending on the pressure of the vapor being adsorbed relative to its saturation vapor pressure (p/p_{sat}). Hence, it is critical to understand alcohol capillarity effects on the adhesion of nano-asperity silicon oxide surfaces.

Atomic force microscopy (AFM) has been used to quantitatively measure the capillary forces exerted by the liquid meniscus at the nano- and micro-scales, directly related to MEMS and other applications [4–10]. Figure 1 shows the pull-off force for silicon oxide surfaces in various alcohol vapor environments measured with AFM tips mounted on low spring constant cantilevers [10]. Of note in Fig. 1 is that starting at the saturation p/p_{sat}, the force increases substantially as p/p_{sat} decreases. There are a number of theoretical models that consider experimentally observed capillary force trends. In the following paragraphs, the assumptions used in these theoretical calculations and their validity will be briefly discussed.

One of the most widely used equations to describe the capillary force is $F_{\mathrm{c}} = 4\pi R\gamma\cos\theta$ where R, γ and θ are the radius of the tip (modeled as a sphere), the liquid surface tension, and the contact angle of the liquid on the solid surface,

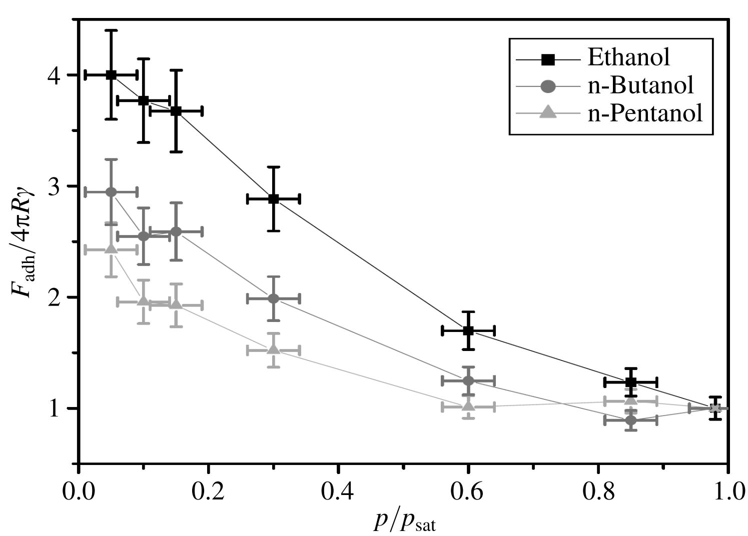

Figure 1. Pull-off force measured with atomic force microscopy for clean SiO_2 surfaces as a function of relative partial pressure (p/p_{sat}) of ethanol, n-butanol, and n-pentanol [10]. The force is normalized with $4\pi R\gamma$ ($R =$ AFM tip radius and $\gamma =$ surface tension of liquid). {Reprinted with permission from the American Chemical Society.}

respectively [11, 12]. This equation originates from the Young–Laplace equation which contains two principal radii of the meniscus (see Section 2.1) through several assumptions. One assumption is that the radius of the tip is much larger than the cross-sectional radius of the liquid meniscus which, in turn, is much larger than the meridional curvature (external curvature) of the meniscus surface [5, 11–13]. However, this assumption is not valid especially for the nano-scale relevant to AFM experiments. He *et al.* extended this model and derived an equation that does not require the large contact area assumption [7]. They found that the capillary force becomes larger than $4\pi R\gamma\cos\theta$ as the size of the tip decreases. In any case, these models predict no vapor pressure dependence of the capillary force, which is inconsistent with experimental results reported in the literature [4–10].

More elegant models use a circular approximation described by Orr *et al.* to calculate the capillary force due to the liquid meniscus without making the aforementioned assumption [14]. In this approximation, the meridional profile of the meniscus is modeled by an arc of a circle (cross section of a torus). Xiao and Qian assumed that the meniscus edges met with the tip and substrate surfaces with finite contact angles and estimated the size of the meniscus using the Kelvin equation at a given vapor partial pressure [5]. This model shows some vapor pressure dependence of the capillary force, but the exact shape deviates from the experimental data.

It should be noted that on clean silicon oxide surfaces, the contact angle of water and short-chain alcohols is near zero (completely wetting). Therefore, assuming a finite contact angle at the meniscus edge is inappropriate especially for water and alcohol condensation on hydrophilic surfaces. Bhushan, Butt and other groups have used the same or similar circular approximation for the case where the contact angles are zero at both tip and substrate surfaces [15, 16]. In this case, however, the theoretical predictions are that the capillary force is the same as $4\pi R\gamma$ (since $\cos\theta = 1$ when $\theta = 0°$) and does not change until the vapor pressure approaches the saturation pressure, where the capillary force diminishes. This prediction is in sharp contrast with Fig. 1 as well as with experimental observations previously reported for silicon oxide surfaces exposed to water and alcohol vapors [4–10, 17].

These theories neglect the role of the *adsorbate film* on the tip and substrate surfaces. The thickness trend of this film *versus* vapor pressure is known as an adsorption isotherm, and can be described by a Langmuir, BET or other isotherm model [18]. As we shall show, incorporating the effect of this film into the theory explains why the capillary force increases much larger than $4\pi R\gamma$ as p/p_{sat} decreases from saturation, i.e., below a value of 1. On most high surface energy solid surfaces (such as oxides and metals), adsorption of water or organic molecules readily occurs from the surrounding gas environments. The thickness of the adsorbate layer can vary from less than one monolayer to several molecular layers depending on the partial pressure of the molecule in the gas phase [19–21]. The adsorbed layer may have different molecular orientation or packing from the bulk liquid [21, 22]. Because both the liquid meniscus and the adsorbed film consist of the same molecules and are in equilibrium with the vapor, the adsorbed film should be considered a continuous film of the condensed phase composing the meniscus. This adsorbate film then acts as the *disjoining layer* in the mechanics terminology [23].

The effects of the disjoining layer in capillary force measurements have been discussed by Mate, White and their colleagues for lubricant films [24, 25]. However, the vapor pressure of lubricant molecules is extremely low. Therefore, the vapor-adsorbate equilibrium can be ignored, and the focus of that work was to calculate the disjoining pressure of the film from the capillary force measured during the stretching of the meniscus with tips attached to high spring constant cantilevers. In their experiments, a lubricant layer of a known thickness is applied to a substrate and the force *versus* displacement curve of an AFM tip of known radius is measured. The force measured during the stretching of the lubricant layer is analyzed to determine the effective meniscus curvature, which is directly related to the Laplace pressure and hence the disjoining pressure [25].

Wei and Zhao calculated the growth rate of a liquid meniscus in humid environments on the substrate and a finite contact angle on the tip surface [26]. They assumed a disjoining layer only on the substrate and calculated the capillary growth kinetics by considering vapor-phase diffusion. Their theory qualitatively supported the experimental results. Asay and Kim recently measured the effect of the vapor-adsorbate equilibrium on the AFM pull-off force measured in water and alcohol vapor environments [9, 10]. Their capillary force model uses the circular approximation with zero contact angles and includes the adsorbate films on both tip and substrate surfaces which are in equilibrium with the vapor. The good agreement between their model and experimental data obtained for alcohol vapors [10] motivated the present work. In the case of water, the agreement is poor and the discrepancy is attributed to the presence of solid-like structured water [9]. Therefore, only alcohol vapors are considered here.

In this paper, the effects of the adsorbate film (disjoining layer) in equilibrium with the vapor are considered by using the exact solution of the Young–Laplace equation for an axisymmetric meniscus (commonly known as a pendular-ring geometry) [14]. It is compared with the circular approximation using a simple trigonometric relation to estimate the meridional and axial radii of the meniscus [9, 10]. Both formulations use the adsorption isotherm and the Kelvin equation [10]. A polynomial fit describing the thickness of the adsorbate layer at a given vapor pressure relative to the saturation pressure, $h(p/p_{\rm sat})$, has been generated to represent the experimentally determined isotherms of alcohols on clean SiO_2 surfaces [10]. The tip radius is varied in the models from 10 nm to 1 μm, mimicking typical AFM experiments. Both models show that as $p/p_{\rm sat}$ decreases from the saturation, the capillary force increases and reaches a maximum at $p/p_{\rm sat} \sim 0.15$. The trend and magnitude calculated from these methods are in agreement with experimentally observed behavior for alcohol vapors. It is also confirmed that when the adsorption isotherm thickness is ignored, the capillary force is fairly insensitive to the alcohol vapor pressure except near the saturation vapor pressure region where the capillary force is predicted to diminish sharply.

2. Theoretical Calculation Details

In Section 2.1, we show that the capillary pressure of the meniscus and the disjoining pressure of the adsorbed layer are equal if both are in thermodynamic equilibrium with the vapor. In Sections 2.2 and 2.3, we derive exact and approximate models for the effect of disjoining pressure on capillary force as a function of p/p_{sat}. The assumptions are that the sphere and substrate are elastically rigid, and that the disjoining layer forms a continuous film. The disjoining layer is the adsorbate film which is in equilibrium with the vapor and the capillary meniscus. The calculation methods and results will be presented and discussed in Section 3, where they will also be compared to each other as well as to the theory which does not include the disjoining layer.

2.1. Equivalence of Capillary and Disjoining Pressures

The fundamental equation of capillarity, the Young–Laplace equation, is derived from a surface curvature argument [18]. Accordingly, a curved liquid–vapor interface supports a pressure difference

$$\Delta P = \gamma / r_{\mathrm{e}}. \tag{1}$$

This quantity is equal to the capillary pressure. Here, the liquid surface tension is γ and the effective radius of curvature of the surface is r_{e} as defined by

$$\frac{1}{r_{\mathrm{e}}} = \frac{1}{r_{\mathrm{a}}} + \frac{1}{r_{\mathrm{m}}}, \tag{2}$$

where r_{a} (the azimuthal radius) and r_{m} (the meridional radius) are the principal radii of curvature of the surface, as shown in Fig. 2(a). These quantities are positive when the center of the radius is inside the meniscus (r_{a}) and negative when outside (r_{m}). The liquid is assumed to be isobaric, meaning that r_{e} is constant along the meniscus surface, while r_{a} and r_{m} may vary along the surface.

The Kelvin equation is derived from thermodynamic equations and the Young–Laplace equation [18]. First, for a reversible process at constant temperature, the effect of the change in mechanical pressure on the free energy G_{f} of a substance is

$$\Delta G_{\mathrm{f}} = \int V_{\mathrm{m}}\, \mathrm{d}P, \tag{3}$$

where V_{m} is the molar volume of the liquid. Assuming constant molar volume of the liquid substance V_{m}, and applying the Young–Laplace equation, equation (1), we obtain

$$\Delta G_{\mathrm{f}} = \gamma V_{\mathrm{m}} / r_{\mathrm{e}}. \tag{4}$$

Thermodynamics relates the free energy of a substance to its vapor pressure. Assuming the vapor to be ideal,

$$\Delta G_{\mathrm{f}} = R_{\mathrm{u}} T \ln(p/p_{\mathrm{sat}}), \tag{5}$$

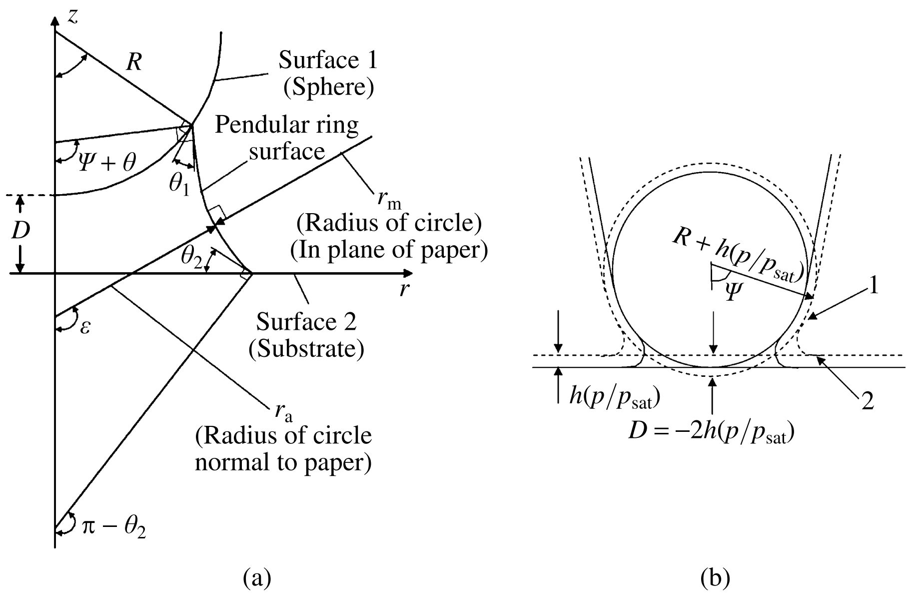

Figure 2. (a) Typical geometry considered for a pendular ring or liquid bridge between a sphere and a flat substrate [30]. {Reprinted with permission from Elsvier.} (b) Modified pendular ring geometry for a system where the equilibrium adsorbate layers are present on both the sphere and the substrate. In this modified geometry, $D = -2h(p/p_{\text{sat}})$. The interpenetration of the sphere into the surface 2 of (a) does not affect the force because the Laplace–Young solution treats only the capillary force and not the contact mechanics problem. In this paper, the force is calculated at point 1. Although individual components (axial surface tension and Laplace pressure) contributing to the capillary force vary with the position, the total capillary force does not vary with the position because the system is in mechanical equilibrium.

where R_{u} is the universal gas constant and T is temperature (K). Equating (4) and (5), and assuming thermodynamic equilibrium, the Kelvin equation [18] is found.

$$r_{\text{K}} = \frac{\gamma V_{\text{m}}}{[R_{\text{u}} T \ln(p/p_{\text{sat}})]}. \tag{6}$$

For example, $r_{\text{K}} = \frac{0.53}{\ln(p/p_{\text{sat}})}$ nm for water at 300 K. At thermodynamic equilibrium, r_{e} equals the Kelvin radius r_{K}, a negative number for $0 < p/p_{\text{sat}} < 1$.

Also, at thermodynamic equilibrium the disjoining pressure $P(h)$ of the adsorbed layer is related to the partial pressure of the vapor by [11],

$$\upsilon P(h) = k_{\text{B}} T \ln(p/p_{\text{sat}}). \tag{7}$$

Here, h is the equilibrium thickness of the film, υ is the liquid film molecular volume, k_{B} is Boltzmann's constant, T is the temperature and p/p_{sat} is the relative vapor pressure. According to Mate [27], the term $\upsilon P(h)$ represents the molecular interaction of the liquid film with the surface relative to that with the bulk liquid, i.e., the Gibbs free energy per molecule.